From Nano-Alloy to Nano-Laminated Interfaces for Highly Stable Alkali Metal Anodes

Parham Pirayesh[1+], Karnpiwat Tantratian[2+], Maedeh Amirmaleki[3,6+], Feipeng Yang[4], Enzhong Jin[1], Yijia Wang[1], Lyudmila V. Goncharova[5], Jinghua Guo[4], Tobin Filleter[3], Lei Chen[2], Yang Zhao[1*]*

[1]Department of Mechanical and Materials Engineering
University of Western Ontario, London, Ontario, N6A 5B9, Canada
Email: Y. Zhao: yzhao628@uwo.ca

[2]Department of Mechanical Engineering
University of Michigan−Dearborn, Dearborn, Michigan 48128, United States
Email: L. Chen: leichn@umich.edu

[3]Department of Mechanical and Industrial Engineering
The University of Toronto, Toronto M5S 3G8, Canada

[4]Advanced Light Source
Lawrence Berkeley National Laboratory, Berkeley, CA, 94720, United States

[5]Department of Physics and Astronomy
University of Western Ontario, London, ON N6A 3K7, Canada

[6]Department of Materials Science and Engineering,
Massachusetts Institute of Technology, Cambridge, MA 02139, United States

+ These authors contributed equally to this work

This is the author manuscript accepted for publication and has undergone full peer review but has not been through the copyediting, typesetting, pagination and proofreading process, which may lead to differences between this version and the Version of Record. Please cite this article as doi: 10.1002/adma.202301414.

Abstract

Metal anodes are considered as the holy grail for the next generation batteries because of their high gravimetric and volumetric specific capacity and low electrochemical potential. However, several unsolved challenges have impeded their practical applications, such as dendrite growth, interface side reaction, dead layer formation and volume change. An electrochemically, chemically, and mechanically stable artificial solid electrolyte interphase (SEI) is key to addressing the aforementioned issue with metal anodes. This study demonstrates a new concept of organic and inorganic hybrid interfaces for both Li and Na metal anodes. Through tailoring the compositions of the hybrid interfaces, we realize the nano-alloy structure to the nano-laminated structure. As a result, the nano-alloy interface ($1Al_2O_3$-1alucone or $2Al_2O_3$-2alucone) presents the most stable electrochemical performances for both Li and Na metal anodes. The optimized thicknesses required for the nano-alloy interfaces for Li and Na metal anodes are different. A cohesive zone model was applied to interpret the underlying mechanism. Furthermore, the influence of the mechanical stabilities of the different interfaces on the electrochemical performances has been investigated experimentally and theoretically. Our approach provides a fundamental understanding and establishes the bridge between mechanical properties and electrochemical performance for alkali metal anodes.

1. Introduction

The next-generation alkali metal batteries, such as Li-metal and Na-metal batteries, have received increasing attention because of their high energy densities[1]. However, several challenges need to be addressed before their practical applications. Firstly, the Li and Na dendrite growth will induce short circuits and cause safety concerns[2]. Secondly, undesired chemical and electrochemical side reactions between highly reactive Li/Na metal with liquid electrolytes lead to unstable solid electrolyte interphase (SEI)[3], which results in large polarization and deteriorates the electrochemical performance. Thirdly, the formation of dendrites and unstable SEI lead to low Coulombic efficiency (CE) and inactive "dead Li/Na" layers[4]. A stable SEI enables uniform Li/Na electrochemical deposition behaviors and enhances electrochemical performances. The unstable SEI layer can promote dendrite growth due to the nonuniform ion flux distribution and non-homogeneous alkali metal depositions,

leading to the large polarization and the decay of the electrochemical performances[5]. Various approaches, such as electrolyte modifications, interface engineering and electrodes/separator designs, have been proposed to stabilize the interface to reduce the dendrite growth, prevent the side reaction and enhance the electrochemical performances[6]. One of the most popular strategies is to design artificial interfaces for Li and Na metal anodes[7]. In the previous study, different artificial interfaces have been reported with improved electrochemical performances and reduced dendrite growth, such as ceramic layers, solid-state electrolyte layers, polymer layers, and hybrid layers[5c, 8].

However, a few questions still remain. How do the composition, structure and properties of the artificial interfaces affect the battery performance? What properties play a major role in cycling stability? For the different alkali metals, will they follow the same design principles for the artificial interfaces? It has been widely studied that the chemical and electrochemical stabilities of the interface can affect electrochemical performances. Recently, the importance of mechanical properties of the interfaces for the electrochemical deposition behavior and performances is gradually recognized[9]. However, how to design a chemically/electrochemically/mechanically stable interface is still an unanswered question. The most widely used inorganic layers, such as metal oxide or solid-state electrolytes, generally have high Young's modules but are often brittle, which leads to crack formation in the inorganic layers during the metal deposition process[10]. The organic polymers with high flexibility are promising candidates to relieve the volume change of Li/Na metal during cycling[11]. However, the dendrites can penetrate the polymer layers due to its low modulus and strength. In this case, there is still a challenge of balancing the multiple mechanical parameters to achieve a mechanically stable interface [12]. In order to tune the mechanical properties of the interface, the most effective approach is to design the organic and inorganic hybrid structures. The organic-inorganic hybrid layers, with different configurations and compositions, present huge interests as interfacial layers for Li and Na metal anodes. Various hybrid structural designs, such as organic-inorganic dual-layer structure, nano-scale gradient structure, cross-linked and multifunctional structure etc., have been proposed[9a, 13]. However, the effects of various hybrid interface structures on electrochemical performance is still being debated. Furthermore, for achieving a long lifetime and dendrite-free structure, there should be a balance between the chemical, electrochemical and mechanical properties of the interfaces.

Different approaches have been reported to fabricate the nanohybrid films, such as self-assembly, chemical vapor deposition and magnetron sputtering, for diverse range of different

applications[14]. However, most of these methods are not suitable for engineering the interface for Li and Na metal anode due to the high reactivities and low melting points of alkali metals. Another challenge is to fabricate the hybrid coating with controlled structure and compositions at the nanoscale. Atomic layer deposition (ALD) and molecular layer deposition (MLD) are unique techniques to achieve nano-hybrid interfaces for alkali metals with excellent coverage, conformity and low deposition temperatures[15]. For example, the elastic modulus of a few nanometers alucone and Al_2O_3 was reported to be 21-37 GPa and ~165 GPa, respectively. It has also been reported that the ALD-Al_2O_3 and MLD alucone alloy or nano-laminated films with varying ratios of ALD and MLD, lead to the tuned elastic modulus and hardness[16]. The composition of the hybrid film can be controlled by varying the relative number of ALD and MLD cycles. when deposition cycles for ALD and MLD processes are large to deposit full monolayers, it is called a "nanolaminate structure". When both ALD and MLD cycles are small, it will generate a homogeneous nano alloy film[16c, 17]. However, there is no demonstration for fabricating the nano-hybrid interfaces with balanced chemical/electrochemical/mechanical properties by tuning the composition of the coating. In addition, the electrochemical metal deposition behavior and performance in different electrolytes are quite different between Li and Na metals. The chemical and physical properties of the different alkali metals may also affect the dendrite formation and electrochemical properties of the interfaces. In this case, the design principles and optimal structures for different alkali metals need to be studied in detail.

Herein, we first propose a new concept of organic and inorganic hybrid interfaces with nano-alloy and nano-laminated structures for Li and Na metal anode. Firstly, the structures, thicknesses and compositions of the hybrid interfaces are precisely controlled by the ALD/MLD process. The structures of nano-alloy to nano-laminated are designed with tuned electrochemical and mechanical properties. Secondly, the optimized composition and thicknesses of the Al_2O_3-alucone alloy interface on the Li and Na metal anodes demonstrate significant enhancement for the electrochemical performances. Thirdly, the surface and interface chemistry of SEI properties and behaviors have been studied in detail by complimentary surface and interface characterization techniques. Finally, the mechanisms have been comprehensively understood by the cohesive zone model and phase-field model. Our study provides the bridge between mechanical properties and electrochemical performance for alkali metal anodes and opens a new window to design the nanostructure interfaces for alkali metal anodes for the next-generation alkali metal batteries.

2. Results and Discussion

The schematic diagram of the nano-hybrid interface is shown in **Figure 1(a)**. Inorganic ALD-deposited Al_2O_3 and MLD-deposited organic alucone are used to form the nano-hybrid structures, for demonstrating the concept. In this study, two key parameters of the nano-hybrid interface, the unit structures and thicknesses, are investigated. Three types of unit structures for nano-hybrid interfaces are fabricated, which are one layer of ALD-deposited Al_2O_3 with one layer of MLD-deposited alucone (1ALD-1MLD), two layers of ALD Al_2O_3 with two layers of MLD alucone (2ALD-2MLD), and five layers of ALD Al_2O_3 with another five layers of MLD alucone (5ALD-5MLD). In addition, for each unit structure, different thicknesses have been further investigated by changing the number of deposition cycles. For example, for the 1ALD-1MLD unit structure, we repeat the deposition for this unit structure for a different number of cycles, including 5, 10, and 25 cycles. The corresponding samples for 1ALD-1MLD unit structures with different thicknesses are named: (1ALD-1MLD)5, (1ALD-1MLD)10 and (1ALD-1MLD)25, respectively. The same naming conversion has been applied to the other two types of unit structures. To demonstrate the unique feature of the rational-designed nano-hybrid interface, both Li and Na metal anodes are used for comparison.

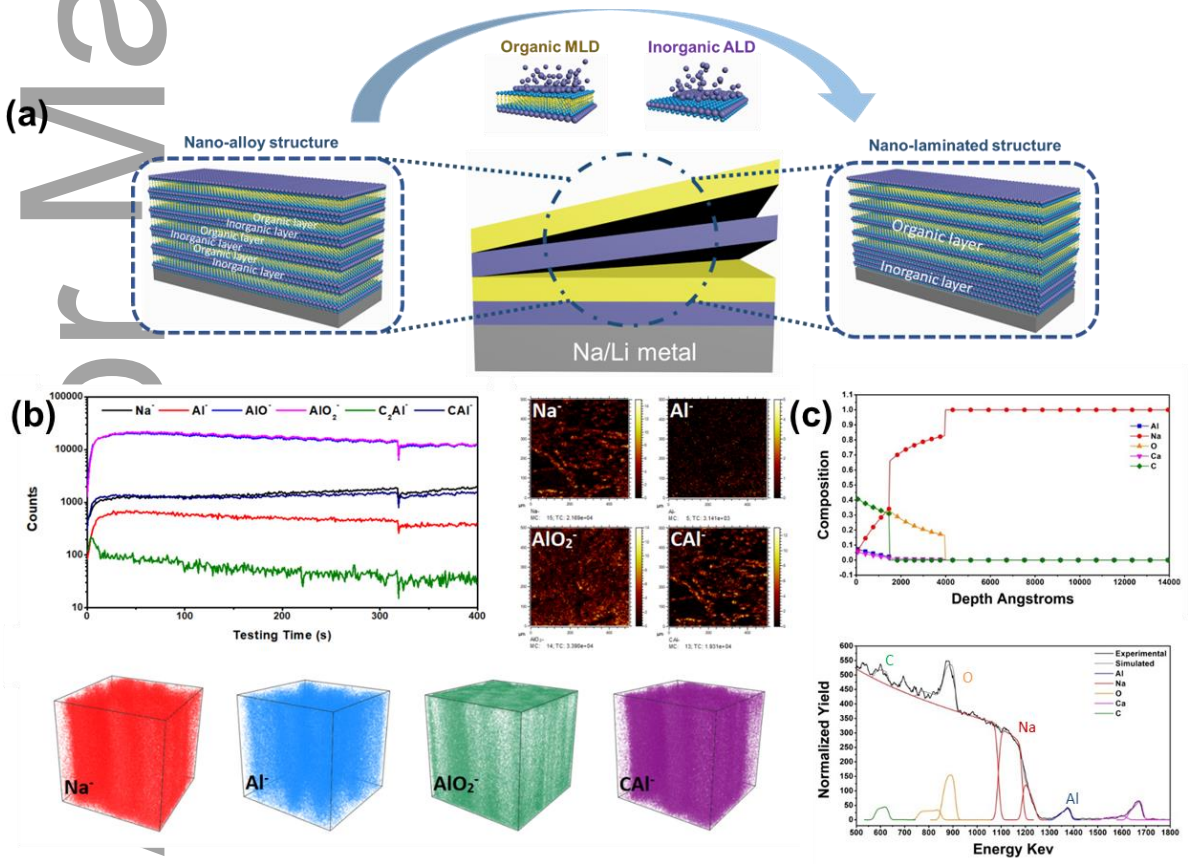

Figure 1 (a) Schematic diagram of the fabrication of the nano-alloy and nano-laminated interfacial structures (b) The TOF-SIMS secondary ion images, the depth profile of various

secondary ion species and corresponding 3D images of Na@(1ALD-1MLD)10; (c) The RBS spectra and calculated depth profiles of Na@(1ALD-1MLD)10.

Several surface characterization methods are applied to understand the surface and interface compositions of the designed nano-hybrid interfaces for both Li and Na metal anodes. The time-of-flight secondary ion mass spectrometry (TOF-SIMS) is performed to probe the composition and the element depth distributions of the nano-hybrid. The TOF-SIMS results of Na@(1ALD-1MLD)10, Na@(2ALD-2MLD)4, and Na@(5ALD-5MLD)2 are shown in **Figure 1(b)**, **Figure S1** and **Figure S2**, respectively. **Figures 1(b)** present the TOF-SIMS depth profiles and chemical ion images of Na^-, Al^-, CAl^-, and AlO_2^- species for Na@(1ALD-1MLD)10. Obvious featured species of CAl^-, (from MLD alucone) and Al^-, AlO_2^- (from both ALD Al_2O_3 and MLD alucone) are observed to identify the deposition of the Al-containing film on the substrates of Na metal. From the depth profiles and corresponding 3D images, it can be observed that all of those species of Al^-, CAl^-, and AlO_2^- distribute from the top surface to the bulk Na metals. Similar phenomena can be observed from both Na@(2ALD-2MLD)4 and Na@(5ALD-5MLD)2, in which the ionic species of Al^-, CAl^-, and AlO_2^- distribute along the surface to the bulk Na. The TOF-SIMS results demonstrate that the inorganic-organic alloy structures are successfully deposited by the hybrid ALD-MLD processes.

The Rutherford backscattering spectrometry (RBS) results for Na@(1ALD-1MLD)10, Na@(2ALD-2MLD)4, and Na@(5ALD-5MLD)2 were further performed, as shown in **Figure 1(c)** and **Figure S (3-4).** RBS Al, C and O surface peaks confirm the successful synthesis of the Al-contained hybrid layers on Na metal. According to the elemental depth profiles obtained by simulating RBS spectra, one can observe that the thicknesses of the nano-hybrid layers for three different configurations are very similar, which is about 200 nm. These results indicate that the sequence of layers of the nano-hybrid structure by ALD/MLD will not affect the total thicknesses of the coating significantly if the total number of ALD-MLD deposition cycles stays the same. Moreover, similar to the TOF-SIMS results, the C spectra from all the samples demonstrate the formation of Al_2O_3-alucone alloy structures, in which the C signals distribute from the top surface to the bulk Na at the same depth as Al.

In addition, the TOF-SIMS results for the nano-hybrid interface coatings on Li metals are shown in **Figures S5-S10**. **Figures S5-S7** present the top surface secondary ion images and their depth profiles and the corresponding 3D reconstructed images for Li@(1ALD-1MLD)10, Li@(1ALD-1MLD)25 and Li@(1ALD-1MLD)50. For the Li@(1ALD-1MLD)10, the AlC_2^-

and $AlOC_2^-$ species derived from MLD alucone distribute along with the AlO^- and AlO_2^- species, which indicates the Al_2O_3-alucone alloy structure and is similar to results for Na@(1ALD-1MLD)10. However, when the total ALD-MLD cycles increase with the same configuration of 1ALD-1MLD (Figures S6 and S7), the signals of AlC_2^- and $AlOC_2^-$ in the depth profiles show fluctuations in the coating layers. The fluctuations of the C-contained species are more obvious for another two configurations of Li@(2ALD-2MLD)25 and Li@(5ALD-5MLD)10, which are shown in **Figures S8 and S9**. The fluctuations of the C-contained species indicate the content change of the alucone layer in the coatings and the formation of the Al_2O_3-alucone alloy with more obvious nano-laminated structures. Furthermore, the (10ALD-10MLD)5 are deposited on Li metal and the TOF-SIMS results are shown in **Figure. S10**. From the 3D reconstructed images of AlC_2^- for Li@(10ALD-10MLD)5, the clear nano-laminated structure of the C-contained layer is observed, resulting from the MLD alucone deposition. In this case, we found that with the control of the unit structures of ALD-MLD deposition, the compositions of the deposited coatings are precisely controlled from Al_2O_3-alucone alloy to Al_2O_3-alucone nano-laminated structures. With the thin unit structures of 1ALD-1MLD and 2ALD-2MLD, it is difficult to form the nano-laminated layered structures since the thickness of the single ALD and MLD layer is at angstrom level. The unit structures of 1ALD-1MLD and 2ALD-2MLD are more like the alloy structure with the Al_2O_3-alucone hybrid coatings. However, when we increase the units to 5ALD-5MLD and 10ALD-10MLD, the structures of the coating layers turn into obvious nano-laminated layered structures. In addition, the soft X-ray Absorption Spectroscopy (XAS) of Near-Edge Structure at Al K edge was carried out to further investigate the composition of the designed samples (**Figure. S11**). As reported in the literature, the main peak for Al K edge for Al_2O_3 at 1564.7 eV is assigned to transitions from the Al 1s orbitals into Al 3p and O 2p antibonding orbitals of t1u symmetry[18]. In the spectrum for the different compositions, this main peak slightly shifts to the low energy of 1564.4 eV. However, the peaks remain in the same position for the alloy structure (Li@(2ALD-2MLD)25) and the nano-laminated structure (Li@(10ALD-10MLD)5), as shown in **Figure S11(a)**. For the alloy structure of (2ALD-2MLD), the increase of the thicknesses (from 10 cycles to 50 cycles) does not affect the local electronic structures of Al (**Figure S11(b)**).

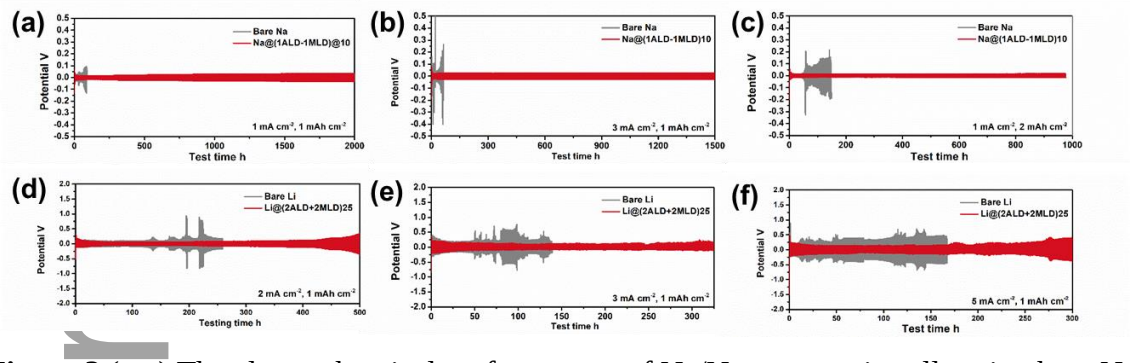

Figure 2 (a-c) The electrochemical performances of Na/Na symmetric cells using bare Na foil and Na@(1ALD-1MLD)10 at different current densities and capacities; (d-f) The electrochemical performances of Li/Li symmetric cells using bare Li foil and Li@(1ALD-1MLD)50 at different current densities.

Symmetrical cells were assembled to evaluate the Na and Li plating/stripping behavior of the different designs of the nano-hybrid layers. **Figure S12** shows the optimization of the different configurations and thicknesses of the nano-hybrid interfaces for the Na metal anodes at the current density of 3 mA cm^{-2} with the capacity of 1 mAh cm^{-2}. The electrochemical performances of the unit structure of 1ALD-1MLD with different thicknesses are presented in **Figure. S12 (a)**. Compared to the performance of bare Na (shown in **Figure. 2 (b)**), the Al_2O_3-alucone alloy coating with the unit of 1ALD-1MLD can significantly improve the cycling stability. The optimized thickness of the 1ALD-1MLD unit with the Al_2O_3-alucone alloy structure is Na@(1ALD-1MLD)10. Another two configurations of 2ALD-2MLD and 5ALD-5MLD are investigated under the same conditions, in which the electrochemical performances are presented in **Figure. S12(b)** and (c), respectively. For the coating with the unit structures of 2ALD-2MLD and 5ALD-5MLD, the thin coatings of Na@(2ALD-2MLD)4 and (5ALD-5MLD)2 show the longest lifetime in their groups. Comparing among the various samples with different units and thicknesses, the Na@(1ALD-1MLD)10 with the Al_2O_3-alucone alloy structure presents the best electrochemical performances at the current density of 3 mA cm^{-2} with the capacity of 1 mAh cm^{-2}. The results indicate that with the optimal thickness, the alloy-based interfaces demonstrate better electrochemical performances compared to the nano-laminated layered structural interface for Na metal anodes.

With the optimized thickness and composition, the Na@(1ALD-1MLD)10 was used to further investigate the battery performance. **Figure. 2(a)** shows the cycling stability of bare Na foil and Na@(1ALD-1MLD)10 at the current density of 1 mA cm^{-2} with the capacity of 1 mAh

cm^{-2}. The initial Na stripping/plating over-potential of bare Na foil is approximately 30 mV and rapidly increases to over 100 mV after ~ 100 h. Then, the short circuit happens with the sudden drop of the overpotential. In contrast, the initial overpotential of the Na@(1ALD-1MLD)10 is about ~ 60 mV and it gradually decreases to about 20 mV after a few cycling, indicating the sodiation process of the Al_2O_3-alucone alloy films. After that, the overpotential of Na@(1ALD-1MLD)10 is extremely stable with a low overpotential of 30 mV after ~ 2000 h without any short circuit. When i the current density is increased to 3 mA cm^{-2} (as shown in **Figure. 2(b)**), the bare Na even has a faster short circuit within 100 h electrochemical cycling. In comparison, the Na@(1ALD-1MLD)10 displays significantly improved stability with a stable overpotential of 30 mV over 1500 h. We also investigate the electrochemical performance with a higher capacity of 2 mAh cm^{-2} with the current density of 1 mA cm^{-2}, as shown in **Figure. 2(c)**. The bare Na displays even worse cycling stability at higher capacity with high overpotential and wildly fluctuating curves. Remarkably, the Na@(1ALD-1MLD)10 shows very stable performances with a low overpotential of 30 mV over 1500 h. The electrochemical impedance spectroscopy (EIS) results for bare Na and Na@(1ALD-1MLD)10 are shown in **Figure S13** for the Nyquits plots before cycling, after 50 cycles, after 100 cycles and after longtime cycles under the current density of 3 mA cm^{-2} with the capacity of 1 mA h cm^{-2}. It is considered that two distinct semicircles are associated with both the SEI/electrode (high frequency) and the charge transfer (CT)/electrical double layer (EDL) (lower frequencies). From **Figure S13 (a)**, it can be observed that the resistance of bare Na slightly increases after 50 electrochemical cycles, however, after 100 cycles and long-time cycles, the resistance of bare Na increases rapidly, indicating the serious side reactions, large impedance interface and dead Na layer formation. As a comparison, the Na@(1ALD-1MLD)10 presents a higher resistance compared to bare Na before cycling, which is consistent with the symmetrical cell performances and due to the non-conductive nature of the Al_2O_3-alucone coating. The resistance of the Na@(1ALD-1MLD)10 after 50 electrochemical plating/stripping decreases and keeps stable after 100 cycles and even after long-time cycling. These results indicate that the Al_2O_3-alucone alloy interlayers have a significant influence on the long-life Na metal anode. Overall, the Al_2O_3-alucone alloy interface of (1ALD-1MLD)10 demonstrates significantly enhanced electrochemical performances and stabilizes the interfaces with low resistances for Na metal anode with high current density or high capacity.

To further prove the concept, the Li-Li symmetrical cells were assembled to evaluate the Li plating/stripping behavior in the carbonate-based electrolyte. The thickness of the interface

is first optimized using the Al_2O_3-alucone alloy structure of (1ALD-1MLD), as shown in **Figure S15**. As shown in **Figure S15**, the optimal thickness of (1ALD-1MLD) alloy interface for Li metal anode in the carbonate-based electrolyte is Li@(1ALD-1MLD)50. Compared to the optimal thickness for the Na metal anode, it requests a much thicker interface layer for the Li metal anode in the carbonate-based electrolyte. With the optimized thickness, we further investigate the structures from alloy to nano-laminated for Li metal anode, as shown in **Figure S16**. We observe that the alloy structure of (2ALD-2MLD)25 presents the best cycling stability compared with the nano-laminated structures. It is worth mentioning that when the structure of the interface tunes from alloy (2ALD-2MLD) to more nano-laminated (5ALD-5MLD and 10ALD-10MLD), the electrochemical performance is even worse, which is consistence with the electrochemical performances for Na metal anode. However, the optimized alloy structures and interface thicknesses for both Li and Na metal anodes are different, which should be the results led by the balances of chemical/electrochemical/mechanical properties in different electrolytes. The comparison of the electrochemical performances for bare Li foil and Li@(2ALD-2MLD)25 is shown in **Figure 2(d-f)**. With the current density of 2 mA cm^{-2} and the capacity of 1 mAh cm^{-2}, the overpotential of bare Li start to fluctuate after 150 h with the overpotential increasing from 100 mV to 800 mV. After 270 h, the short circuit happens for the bare Li foil. However, for the Li@(1ALD-1MLD)50, the cell is very stable with the overpotential of 80 mV over 500 h. When increasing the current density to 3 mA cm^{-2} and 5 mA cm^{-2} (**Figure 2 (e, f)**), the Li(1ALD-1MLD)50 displays significantly improved electrochemical performances with low overpotential and longer lifetime compared to the bare Li foil without coatings.

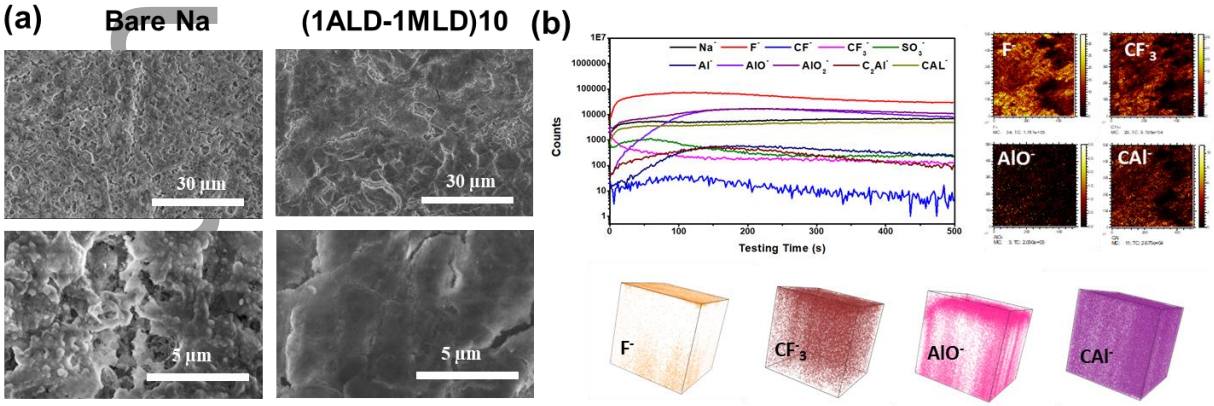

Figure 3 Top-view SEM images of (a) bare Na foil and Na@(1ALD-1MLD)10 after electrochemical cycling (50 cycles); (b) The TOF-SIMS depth profiles and corresponding 3D reconstructed images of Na@(1ALD-1MLD)10 after electrochemical cycling.

To understand the influence of the Al_2O_3-alucone alloy interface on the Na deposition behavior, the morphology and surface composition of Na metal was investigated by different characterizations. **Figure 3** and **Figures S17-S18** show the SEM images of bare Na foil and Na@(1ALD-1MLD)10 after electrochemical cycling of 50 cycles and long cycles at the current density of 1 mA cm^{-2} with a capacity limit of 1 mAh cm^{-2}. From **Figure 3(a)** and **Figure. S17**, we can observe that mossy Na and dead Na layers are formed within 50 cycles, becoming more significant after longer cycling. With long electrochemical cycles (**Figure S17**), long and deep cracks are formed with a rougher surface on the Li, which causes the increase of polarization in the cells and eventually leads to the short-circuit of the batteries. On the contrary, the morphologies of the Na@(1ALD-1MLD)10 after cycling are different, as shown in **Figure 3(b)** and **Figure S18**. The surfaces of the Na@(1ALD-1MLD)10 are much smoother with less mossy Na and crack formation after 50 cycles and long cycles. The mossy/dendritic Na growth and dead Na formation are effectively prevented with the Al_2O_3-alucone alloy interfaces, which leads to significantly improved electrochemical performances. To further study the Na deposition behavior, the Cu foils (with and without coating) are used as counter electrodes. **Figure S19** shows the SEM images of bare Cu foil and Cu@(1ALD-1MLD)10 with electrochemical deposition of different capacities of 0.1 mAh cm^{-2} and 1 mAh cm^{-2} at the current density of 1 mA cm^{-2}. It can be clearly seen from **Figure S19 (a)** that the morphology of the deposited Na on bare Cu foil during the initial nuclear process with the capacity of 0.1 mAh cm^{-2} is non-uniform with mossy Na and crack formation. With an increasing capacity to 1 mAh cm^{-2}, the surface of the deposited Na turns rougher and large holes/cracks form during the deposition process. On the contrary, the Na deposition on the Cu@(1ALD-1MLD)10 is very smooth without any mossy and dendrite formation from the nuclear stage to the higher capacity, as shown in **Figure S19 (b)**. The deposition behavior study demonstrates that the designed nano-alloy interface is enabled to reduce the Na dendrite growth and is expected to improve the electrochemical performances.

Besides the morphology, the compositions of the interface are critical for the metal deposition and electrochemical performances. The TOF-SIMS is carried out to understand the chemical composition of the interface after plating/stripping. In **Figure S20,** the TOF-SIMS

results of surface chemical ion images, depth profiles and corresponding 3D reconstructed images for bare Na foil after 50 cycles of plating/stripping under the conditions of 1 mA cm^{-2}/1 mAh cm^{-2} are displayed. For cycled bare Na foil (**Figure S20**), the surface is covered with by-products from the side reactions between Na metal with electrolytes, presenting the strong signal of F^- and SO_3^-. As shown in **Figure 3 (b)**, the Al_2O_3-alucone alloy coating remains on the surface of Na metal after cycling and has small changes compared to the TOF-SIMS result before cycling (**Figure 1(b)**). The TOF-SIMS results demonstrate that the Al_2O_3-alucone alloy interface is robust and chemical/electrochemical stable during electrochemical cycling. Similarly, the TOF-SIMS results for bare Li foil and Li@(1ALD-1MLD)50 after 50 cycles of electrochemical plating/stripping are presented in **Figures S21** and **S22**, respectively. The pristine Li shows deep penetration of F from electrolyte with a long sputtering time (over 1000 s), which is related to the thick dead Li layer formation. In contrast, for the Li@(1ALD-1MLD)50 after cycling (**Figure S22**), the Al_2O_3-alucone alloy interface is very stable and remains with a similar structure compared to the coating before cycling. The XAS at Al K-edge was performed for Li@(2ALD-2MLD)25 after cycling. After cycling, the XAS spectra of Al K-edge (**Figure S23**) become broader, with the peak shifts to higher energy compared to that of before cycling. However, it still confirms that (2ALD-2MLD)25 interface is a stable protective layer during cycling. The integration of organic compounds, such as zincone and titanicone, into inorganic layers can lead to the formation of polymer chains containing benzene rings, specifically $(\text{-Zn-O-Benzene-O})_n$ and $(\text{-Ti-O-Benzene-O})_n$ [19]. DFT calculations have shown that these polymer chains are the key to reducing the energy barrier for Li-ion migration[19]. Similarly, in this work, the addition of the alucone organic layer expectedly containing $(\text{-Al-O-CH}_x\text{-O})_n$ chains could have similar potential to enhance Li and Na ion migration at the interface.

We further investigate the influence of mechanical properties on the interfaces. First, we understand the effect of the thickness of the film on the mechanical properties using the 1ALD-1MLD alloy structure as an example. The mechanical performance of the different film thicknesses of 1ALD-1MLD alloy structures was evaluated using the AFM deflection technique where the centre of a free-standing film is deflected with predefined force and the film deflection from the applied force is detected[9a, 9c, 20]. A holey silicon nitride TEM grid with a hole diameter of 2.7 μm covered with monolayer graphene as a support layer was used to deposit the ALD and MLD films. The mechanical properties of single-layer graphene were found to dominate the mechanical performance of thin layers up to 3 nm thickness, therefore

we evaluated the mechanical performance of (1ALD-1MLD)10 and (1ALD-1MLD)25 and (1ALD-1MLD)50 with 4-20 nm thickness. All mechanical tests were conducted using an Asylum MFP-3D AFM. The cantilever with a diamond tip (NadiaProbes, Catalogue #: ND-DYIRS-5) was calibrated using Sader's method with a normal spring constant of 35 Nm^{-1}. For elastic studies, the films were deflected to small force ranges < 60 nN while the films were deflected to failure at higher force levels to study the failure. At least ten samples were collected for elastic and failure behaviour for each film. For all of the films, the elastic response was found to be consistent and repeatable. No significant hysteresis was observed between loading-unloading curves, implying no obvious slippage between deposited layers and graphene substrate. Due to the covalent bonding inherent to the deposition process, good adhesion between ALD and MLD layers is expected, and no hysteresis was observed for deflection tests. **Figure S24** represents the elastic behaviour of the (1ALD-1MLD)10 and (1ALD-1MLD)25 and (1ALD-1MLD)50 films. As expected, the in-plane stiffness of the alloy structure increased with the thickness (stiffness is related to the slope of the force-deflection curve). The films deflected to failure which is identified by abrupt force drop to or beyond 20% of maximum force. Failure force-deflection representative curves of the (1ALD-1MLD)10 and (1ALD-1MLD)25 and (1ALD-1MLD)50 alloy films are shown in **Figure 24** (b). The elastic and failure results showed that the (1ALD-1MLD)50 remains stiff, from the slope of (F–δ) curve, during the entire loading stage to failure. Interestingly, for (1ALD-1MLD)10 and (1ALD-1MLD)25 films the slope of F–δ curve was observed to significantly increase at higher forces and as such the film exhibited higher stiffness. The increased stiffness is likely due to strain hardening from the alignment of the polymer network in the (1ALD-1MLD) alloy during plastic deformation which is noticeable for smaller thicknesses. The toughness values of the films were calculated based on the area under the F-δ curve below the failure point. In **Figure S24 (c)**, the $F_{Facture}$ and toughness values of the alloy structures normalized to the film thinness are presented. The trend in the normalized $F_{Fracture}$ and toughness to thickness implies that a higher amount of forces is required to fail the thinner films; therefore, the normalized toughness decreases with thickness due to the higher volume and higher number of defects under the tip at failure. These mechanical results indicate that the thinner films with higher toughness likely will fail under higher stress levels and can show more flexibility at the interface with Na compared to thicker films, which is in agreement with their electrochemical performances in this work.

We further used the same AFM deflection technique mentioned before to study the mechanical performance of (1ALD-1MLD)50, (2ALD-2MLD)25 alloy film and (5ALD-

5MLD)10 nano-laminated film with a similar thickness of ~20 nm, which are used as protective layers for Li metal anodes (As shown in **Figure S25)**. As discussed above, for the Li metal anode, the optimized thickness and composition for electrochemical performance are (2ALD-2MLD)25. Interestingly, when increasing the film thicknesses to 20 nm, the mechanical performances of the films from the alloy structure to the nano-laminated structure are not as strong as the films with a thin thickness (like 4 nm), which is likely due to the increased volume of the films as well as the number of defects under the AFM tip. However, the nanoalloy structure of (2ALD-2MLD)25 still presents higher forces and higher stiffness compared to the other two films, which is constant with the electrochemical performances of the Li metal anode. Herein, although the optimized thicknesses and compositions for Li and Na metals are quite different, the mechanical properties still play an important role in affecting the electrochemical stabilities.

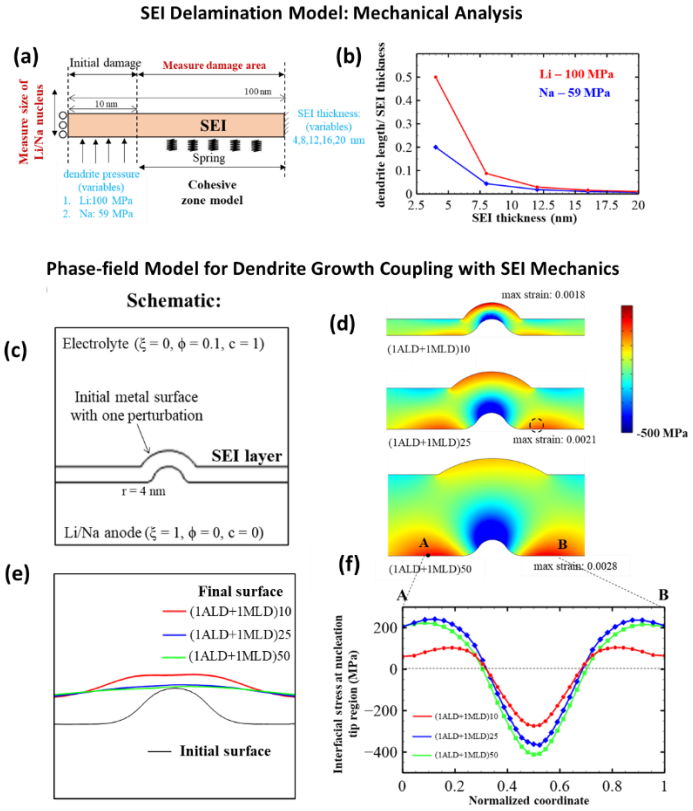

Figure 4 SEI delamination model based on mechanical analysis: (a) schematic with initial and boundary conditions (b) the plot of the SEI thicknesses against the resulting dendrite nucleation length (normalized with the SEI thicknesses); Phase-filed model for dendrite growth coupling with SEI mechanics: (c) schematic of the simulation with initial and boundary conditions (d) stress distribution on three SEI thicknesses: (1ALD+1MLD)10, (1ALD+1MLD)25, and (1ALD+1MLD)50. (e) the resulting anode surfaces due to the

mechanical suppression by each SEI thickness. (f) 1D interfacial stress distribution near the perturbation region from point A to B.

As observed in the previous section, the optimal thickness of SEI for Li is 20 nm, while it is 4 nm for Na. This section aims to explain why Li needs a thicker SEI layer to effectively suppress dendrite. To do so, the mechanics of the SEI delamination is simulated with a cohesive zone model (CZM). **Figure 4(a)** shows the geometry and initial/boundary conditions of the stress equilibrium equation. The initial damage area refers to the region where the SEI is fully delaminated from the anode surface due to the Li/Na dendrite initiation and is under mechanical pressure from Li/Na dendrite nucleation pushing outward. The undamaged area is modelled by CZM with the bilinear form of traction-separation law[21] (Supporting Information for more details). The physics simulation is run in, a finite element software, COMSOL Multiphysics. The magnitude of pressure that Li/Na acting on the SEI is evaluated through the following thermodynamics relationship[22]:

$$\sigma V_m = F\Delta\emptyset, \tag{1}$$

where σ is mean stress, V_m is the molar volume of the anode, F is Faraday constant, and $\Delta\emptyset$ is the overpotential that drives the reaction. Under the same charging rate, $\Delta\emptyset$ is assumed constant, and thus the mechanical pressure is solely a function of V_m, which varies from one to another material. Experimental characterizations, **Figure S26**, show that under the same charging conditions (3 mA cm^{-2}, 5 mAh cm^{-2}), the thickness ratio of deposited Li over the deposited Na ($V_{m,Li}/\ V_{m,Na}$) is 0.59. Therefore, the ratio of pressure exerted by deposited Na and Li (σ_{Li}/σ_{Na}) is 1.82. Here, in the simulation, it is assumed that σ_{Li} is 100 MPa; thus, σ_{Na} is 59 MPa. The studied range of SEI thickness is from 4 to 20 nm. The displacement of the left boundary in the y-direction is associated with the dendrite length and is measured when the system reaches mechanical equilibrium. **Figure 4(b)** shows that when the SEI thickness is 4 nm, the Li dendrite length is much larger than the Na dendrite. And to achieve a similar suppression performance (same length of dendrites), Li would obviously require a thicker SEI than Na due to a larger induced mechanical stress.

Next, we aim to simulate how each (1ALD+1MLD) thickness works against dendrite nucleation through the phase-field model for dendrites coupled with SEI mechanics. This phase-field model is an extension of L.Chen and K.Tantratian works[23]. More details are

available in Supporting Information. **Figure 4(c)** shows the initial morphology of the anode surface with a perturbation radius of 4 nm. In this mechano-electrochemical modeling, the velocity of the moving Li/SEI interface is the boundary condition that causes the stress distribution in the SEI domain. Meanwhile, the interfacial stress at Li/SEI interface plays a part in controlling the plating behavior: interfacial tensile stress promotes deposition rate, while interfacial compressive stress suppresses deposition reaction. Each (1ALD+1MLD) thickness has distinct mechanical properties due to the size scale effect, and the elastic modulus of each one is extracted from **Figure S24.** The negative overpotential of 0.1 V is applied to simulate plating behavior. Stress distributions in the SEI as well as the resulting surface morphologies are captured at the end of the simulations.

Figure 4(e) shows how different SEI thicknesses smoothen the anode surface during the plating process. The black line represents the initial anode surface, with one perturbation. As a result of plating, the final anode surface rises up, but the morphologies are different from one to another case. (1ALD+1MLD)25, and (1ALD+1MLD)50 both result in a very smooth surface, while the perturbation is not well suppressed in the case of (1ALD+1MLD)10. This is due to the different magnitudes of mechanical stress at the interface, **Figure 4(d)** and **Figure 4(f)**. (1ALD+1MLD)25 and (1ALD+1MLD)50 possess a similar magnitude of interfacial stress, while the interfacial stress in (1ALD+1MLD)10 is lower. The mechanical suppression mechanism works by slowing down the deposition rate at the tip due to compressive stress while promoting the plating reaction at the valleys due to tensile stress. However, if the interfacial mechanical stress is too low, the impact of mechanics on the electrochemical reaction is not significant, and rough surfaces are not effectively alleviated, like in the case of (1ALD+1MLD)10. As a result, a thicker SEI layer tends to have better dendrite suppression performance. Nevertheless, it is important to note that high tensile stress at the interface can also cause SEI delamination, leading to other interfacial issues. Therefore, the thickness of the SEI layer must be optimized to balance the mechanical suppression effect and the potential delamination issue.

Based on the discussion above combing electrochemical performance, mechanical property measurements, and theoretical modelling, we have provided a comprehensive understanding on the electrochemical/chemical/mechanical stability of the interfaces for metal anodes. 1) For both Li and Na metal anodes, the nano-alloy structure interfaces present the best electrochemical performances and the nano-alloy interfaces are electrochemically and chemically stable after cycling. 2) However, the thicknesses of the nano-alloy interfaces

required for Li and Na metal anodes are quite different, in which a thicker interface is essential for Li metal and a thinner coating is strong enough for Na metal. A cohesive zone model is proposed to explain the mechanism. 3) The mechanical behaviour of the hybrid films is affected by both thickness and configuration. Although the thin nano-alloy film demonstrates a higher toughness and average failure force, the thick nano-alloy interface provides a higher interfacial stress and smooth surface based on the phase-field modelling.

Conclusion

In this study, we demonstrate a new concept of organic and inorganic hybrid interfaces for both Li and Na metal anodes. By controlling the compositions, we realize the nano-alloy structure to the nano-laminated structure. As a result, the nano-alloy interface presents the most stable electrochemical performances for both Li and Na metal anodes. The thicknesses of the nano-alloy interfaces required for Li and Na metal anodes are different and the mechanism is understood by a cohesive zone model. Furthermore, the influence of the mechanical stabilities of the different interfaces on the electrochemical performances has been investigated experimentally and theoretically. Our approach provides a fundamental understanding and establishes the bridge between mechanical properties and electrochemical performance for alkali metal anodes. In addition, a comprehensive understanding of the electrochemical/chemical/mechanical stability of the interfaces for metal anodes has been studied by combing experimental measurements and theoretical modelling. We believe that this work can not only open a new window on the design of the electrochemical/chemical/mechanical stable interfaces for alkali metal but also provides new insight into the mechanical effects of electrochemical metal depositions.

Acknowledgments

This research was supported by the Natural Science and Engineering Research Council of Canada (NSERC), the Canada Foundation for Innovation (CFI), and the University of Western Ontario (UWO). We gratefully acknowledge Dr. Heng-Yong Nie for his help in the discussion on TOF-SIMS results. We would like to acknowledge the technical expertise of Mr. Jack Hendriks at the Western Tandetron Accelerator Facility. This research used resources of the Advanced Light Source, a DOE Office of Science User Facility under contract no. DE-AC02-05CH11231.

Reference

[1] a)Y. Ding, Z. P. Cano, A. Yu, J. Lu, Z. Chen, *Electrochemical Energy Reviews* **2019**, 2, 1; b)Y. Zhang, T.-T. Zuo, J. Popovic, K. Lim, Y.-X. Yin, J. Maier, Y.-G. Guo, *Materials Today* **2020**, 33, 56.

[2] W. Yao, P. Zou, M. Wang, H. Zhan, F. Kang, C. Yang, *Electrochemical Energy Reviews* **2021**, 4, 601.

[3] a)H. Wang, Y. Liu, Y. Li, Y. Cui, *Electrochemical Energy Reviews* **2019**, 2, 509; b)B. Sun, P. Xiong, U. Maitra, D. Langsdorf, K. Yan, C. Wang, J. Janek, D. Schroder, G. Wang, *Adv Mater* **2020**, 32, e1903891.

[4] a)C. Zhao, Y. Lu, J. Yue, D. Pan, Y. Qi, Y.-S. Hu, L. Chen, *Journal of Energy Chemistry* **2018**, 27, 1584; b)Y. Zhao, K. R. Adair, X. Sun, *Energy & Environmental Science* **2018**, 11, 2673.

[5] a)B. Sun, P. Li, J. Zhang, D. Wang, P. Munroe, C. Wang, P. H. L. Notten, G. Wang, *Adv Mater* **2018**, e1801334; b)F. He, W. Tang, X. Zhang, L. Deng, J. Luo, *Adv Mater* **2021**, 33, e2105329; c)A. Hu, W. Chen, X. Du, Y. Hu, T. Lei, H. Wang, L. Xue, Y. Li, H. Sun, Y. Yan, J. Long, C. Shu, J. Zhu, B. Li, X. Wang, J. Xiong, *Energy & Environmental Science* **2021**, 14, 4115.

[6] a)D. H. Liu, Z. Bai, M. Li, A. Yu, D. Luo, W. Liu, L. Yang, J. Lu, K. Amine, Z. Chen, *Chem Soc Rev* **2020**, 49, 5407; b)H. Wang, C. Wang, E. Matios, W. Li, *Angew Chem Int Ed Engl* **2018**, 57, 7734.

[7] Z. Han, C. Zhang, Q. Lin, Y. Zhang, Y. Deng, J. Han, D. Wu, F. Kang, Q. H. Yang, W. Lv, *Small Methods* **2021**, 5, e2001035.

[8] a)G. Jiang, K. Li, F. Yu, X. Li, J. Mao, W. Jiang, F. Sun, B. Dai, Y. Li, *Advanced Energy Materials* **2020**, 11; b)T. Wang, Y. Hua, Z. Xu, J. S. Yu, *Small* **2022**, 18, e2102250.

[9] a)Y. Zhao, M. Amirmaleki, Q. Sun, C. Zhao, A. Codirenzi, L. V. Goncharova, C. Wang, K. Adair, X. Li, X. Yang, F. Zhao, R. Li, T. Filleter, M. Cai, X. Sun, *Matter* **2019**, 1, 1215; b)Z. Yu, Y. Cui, Z. Bao, *Cell Reports Physical Science* **2020**, 1, 100119; c)Y. Sun, M. Amirmaleki, Y. Zhao, C. Zhao, J. Liang, C. Wang, K. R. Adair, J. Li, T. Cui, G. Wang, R. Li, T. Filleter, M. Cai, T. K. Sham, X. Sun, *Advanced Energy Materials* **2020**, 10, 2001139; d)Y. Liu, Y.-K. Tzeng, D. Lin, A. Pei, H. Lu, N. A. Melosh, Z.-X. Shen, S. Chu, Y. Cui, *Joule* **2018**, 2, 1595.

[10] A. L. Davis, R. Garcia-Mendez, K. N. Wood, E. Kazyak, K.-H. Chen, G. Teeter, J. Sakamoto, N. P. Dasgupta, *Journal of Materials Chemistry A* **2020**, 8, 6291.

[11] a)D. Wang, H. Liu, F. Liu, G. Ma, J. Yang, X. Gu, M. Zhou, Z. Chen, *Nano Lett* **2021**, 21, 4757; b)Y. Sun, Y. Zhao, J. Wang, J. Liang, C. Wang, Q. Sun, X. Lin, K. R. Adair, J. Luo, D. Wang, R. Li, M. Cai, T. K. Sham, X. Sun, *Adv Mater* **2019**, 31, e1806541; c)Z. Xu, J. Yang, T. Zhang, L. Sun, Y. Nuli, J. Wang, S. i. Hirano, *Advanced Functional Materials* **2019**, 1901924; d)Z. Huang, S. Choudhury, N. Paul, J. H. Thienenkamp, P. Lennartz, H. Gong, P. Müller - Buschbaum, G. Brunklaus, R. Gilles, Z. Bao, *Advanced Energy Materials* **2021**, 12, 2103187.

[12] T. Krauskopf, F. H. Richter, W. G. Zeier, J. Janek, *Chem Rev* **2020**, 120, 7745.

[13] a)Y. Gao, Z. Yan, J. L. Gray, X. He, D. Wang, T. Chen, Q. Huang, Y. C. Li, H. Wang, S. H. Kim, T. E. Mallouk, D. Wang, *Nat Mater* **2019**, 18, 384; b)Y. Sun, C. Zhao, K. R. Adair, Y. Zhao, L. V. Goncharova, J. Liang, C. Wang, J. Li, R. Li, M. Cai, T.-K. Sham, X. Sun, *Energy & Environmental Science* **2021**, 14, 4085; c)Y. Zhao, G. Li, Y. Gao, D. Wang, Q. Huang, D. Wang, *ACS Energy Letters* **2019**, 4, 1271.

[14] a)X. Jin, T. H. Gu, N. H. Kwon, S. J. Hwang, *Adv Mater* **2021**, 33, e2005922; b)O. I. Kalaoglu-Altan, B. K. Kayaoglu, L. Trabzon, *iScience* **2022**, 25, 103825; c)H. j. Kwon, H. Ye,

Y. Baek, J. Hong, R. Wang, Y. Choi, I. Lee, C. E. Park, S. Nam, J. Kim, S. H. Kim, *Advanced Functional Materials* **2020**, 31; d)S. T. Mahmud, M. M. Hasan, S. Bain, S. T. Rahman, M. Rhaman, M. M. Hossain, M. Ordu, *ACS Materials Letters* **2022**, 4, 1174.
[15] a)Y. Cao, X. Meng, A. Li, *Energy & Environmental Materials* **2020**, 4, 363; b)Y. Zhao, X. Sun, *ACS Energy Letters* **2018**, 3, 899; c)Y. Zhao, L. Zhang, J. Liu, K. Adair, F. Zhao, Y. Sun, T. Wu, X. Bi, K. Amine, J. Lu, X. Sun, *Chem Soc Rev* **2021**, 50, 3889.
[16] a)B. H. Lee, V. R. Anderson, S. M. George, *Chemical Vapor Deposition* **2013**, 19, 204; b)B. H. Lee, V. R. Anderson, S. M. George, *ACS Appl Mater Interfaces* **2014**, 6, 16880; c)B. H. Lee, B. Yoon, V. R. Anderson, S. M. George, *The Journal of Physical Chemistry C* **2012**, 116, 3250; d)B. Yoon, B. H. Lee, S. M. George, *The Journal of Physical Chemistry C* **2012**, 116, 24784.
[17] a)J. W. Elam, S. M. George, *Chemistry of Materials* **2003**, 15, 1020; b)K. Gregorczyk, M. Knez, *Progress in Materials Science* **2016**, 75, 1; c)B. H. Lee, B. Yoon, A. I. Abdulagatov, R. A. Hall, S. M. George, *Advanced Functional Materials* **2013**, 23, 532.
[18] E. Jin, K. Tantratian, C. Zhao, A. Codirenzi, L. V. Goncharova, C. Wang, F. Yang, Y. Wang, P. Pirayesh, J. Guo, L. Chen, X. Sun, Y. Zhao, *Small* **2022**, 18, e2203045.
[19] J. B. Fang, Y. Q. Cao, S. Z. Chang, F. R. Teng, D. Wu, A. D. Li, *Advanced Functional Materials* **2021**, 32.
[20] M. Amirmaleki, T. Cui, Y. Zhao, J. Tam, A. Goel, Y. Sun, X. Sun, T. Filleter, *Nano Lett* **2021**, 21, 437.
[21] K.-J. Lee, H.-J. Yang, K.-C. Chen, *Applications in Engineering Science* **2022**, 9.
[22] Y. He, X. Ren, Y. Xu, M. H. Engelhard, X. Li, J. Xiao, J. Liu, J. G. Zhang, W. Xu, C. Wang, *Nat Nanotechnol* **2019**, 14, 1042.
[23] a)L. Chen, H. W. Zhang, L. Y. Liang, Z. Liu, Y. Qi, P. Lu, J. Chen, L.-Q. Chen, *Journal of Power Sources* **2015**, 300, 376; b)K. Tantratian, H. Yan, K. Ellwood, E. T. Harrison, L. Chen, *Advanced Energy Materials* **2021**, 11.

TOC

A new concept of organic and inorganic hybrid interfaces is proposed for both Li and Na metal anodes, tailoring the compositions from the nano-alloy structure to the nano-laminated structure. The required thicknesses for nano-alloy interfaces differ between Li and Na metal anodes, and the mechanical stabilities of the interfaces affect electrochemical performances.